ACS APPLIED MATERIALS & INTERFACES

Research Article

Cite This: ACS Appl. Mater. Interfaces 2018, 10, 27840−27849

www.acsami.org

Ultraviolet Light-Induced Persistent and Degenerated Doping in MoS_2 for Potential Photocontrollable Electronics Applications

Rongjie Zhang,[†] Zhijian Xie,[‡] Chunhua An,[†] Shuangqing Fan,[†] Qiankun Zhang,[†] Sen Wu,[†] Linyan Xu,[†] Xiaodong Hu,[†] Daihua Zhang,[†] Dong Sun,[‡,§] Jian-Hao Chen,[‡,§] and Jing Liu*[,†]

[†]State Key Laboratory of Precision Measurement Technology and Instruments, School of Precision Instruments and Opto-electronics Engineering, Tianjin University, No. 92 Weijin Road, Tianjin 300072, China

[‡]International Center for Quantum Materials, School of Physics, Peking University, No. 5 Yiheyuan Road, Beijing 100871, China

[§]Collaborative Innovation Center of Quantum Matter, Beijing 100871, China

Supporting Information

ABSTRACT: Efficient modulation of carrier concentration is fundamentally important for tailoring the electronic and photoelectronic properties of semiconducting materials. Photoinduced doping is potentially a promising way to realize such a goal for atomically thin nanomaterials in a rapid and defect-free manner. However, the wide applications of photoinduced doping in nanomaterials are severely constrained by the low doping concentration and poor stability that can be reached. Here, we propose a novel photoinduced doping mechanism based on the external photoelectric effect of metal coating on nanomaterials to significantly enhance the achievable doping concentration and stability. This approach is preliminarily demonstrated by an MX_2 (M is Mo or Re; X is S or Se) nanoflake modified through a simple process of sequentially depositing and annealing an Au layer on the surface of the flake. Under ultraviolet (UV) light illumination, the modified MX_2 achieves degenerated n-type doping density of 10^{14} cm^{-2} rapidly according to the experimentally observed $>10^4$ times increment in the channel current. The doping level persists after the removal of UV illumination with a nonobservable decrease over 1 day in vacuum (less than 23% over 7 days under an ambient environment). This photoinduced doping approach may contribute a major leap to the development of photocontrollable nanoelectronics.

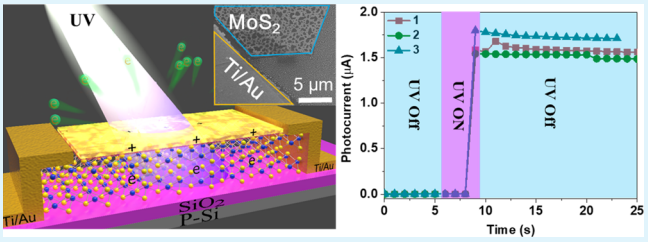

KEYWORDS: *transition metal dichalcogenides, photoinduced doping, external photoelectric effect, gold coating, persistent photocurrent*

INTRODUCTION

Efficient modulation of carriers in semiconducting materials is the foundation to implement various functional electronic[1,2] and optoelectronic devices.[3−5] As the thickness of semiconducting materials decreases to the atomic scale, the efficient carrier modulation not only becomes more critical but also confronts numerous unprecedented challenges. Transition metal dichalcogenides (TMDs), a major subgroup of the atomically thin two-dimensional material family, mainly possess semiconducting properties and thus necessitate competent methods to modulate the carrier concentration to enable nanoscale van der Waals homo-/heterojunctions and functional devices.[6,7] Conventional doping technologies that are applicable to TMDs, such as substitution of transition metal by other elements,[8−11] ion implantation,[12] and plasma treatment,[13,14] may alter and/or introduce abundant defects to the intrinsic lattice structure, which diminishes the carrier mobility of TMDs. Other defect-free doping approaches reported recently are based on charge transfer between TMDs and gases,[15,16] ions,[17] nanoparticles,[18] etc. These methods, however, usually suffer from long-term stability issue[19,20] and involve enduring solution-based processes, which are hardly compatible with standard complementary metal−oxide−semiconductor processes.

In contrast, photoinduced doping is considered to be an effective approach to provide rapid and defect-free doping.[21−23] The working mechanism of photoinduced doping is generally based on the formation of electron−hole pairs in the photoabsorption layer under photoillumination and subsequent charge transfer into the conduction channel,[21] which modulates the carrier concentration of the target material without increasing the Coulombic scattering from space charges. To preserve the doping effect after the removal of photoillumination, a dielectric layer is usually applied above the conduction channel to introduce interface carrier trap-states[21,24] to prevent electron−hole recombination. In this mechanism, the number of carriers generated in the photon-absorption layer and the populated trap-state density largely

Received: May 3, 2018
Accepted: July 31, 2018
Published: July 31, 2018

DOI: 10.1021/acsami.8b07196
ACS Appl. Mater. Interfaces 2018, 10, 27840−27849

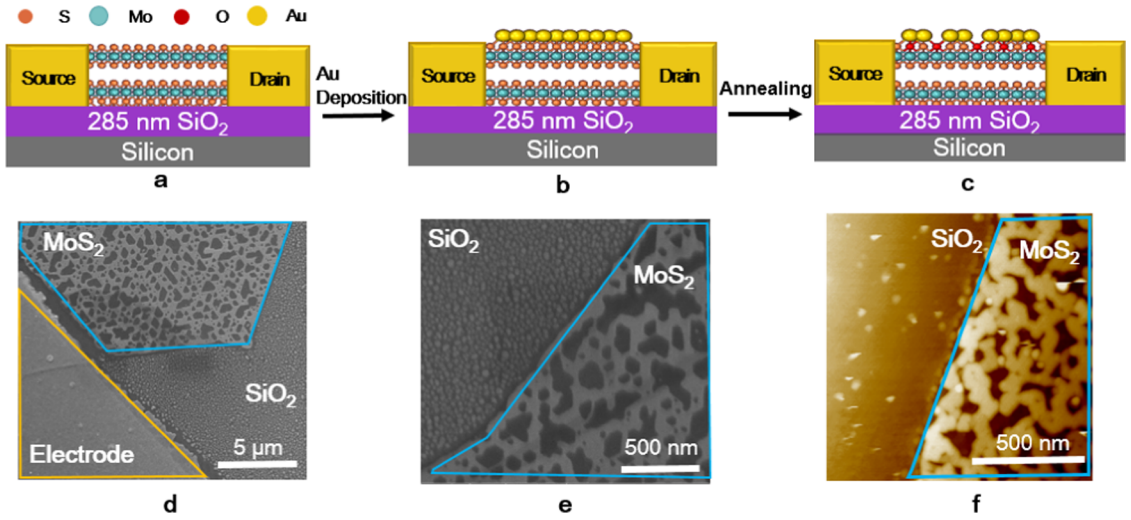

Figure 1. Schematic of device fabrication. (a) Bare MoS_2 FET, (b) deposition of the 6 nm Au film on MoS_2 FET, and (c) annealing of Au-deposited MoS_2 FET under 350 °C for 30 min. (d, e) SEM images showing the morphology of Au film on MoS_2, SiO_2, and electrode after annealing. (f) AFM image showing the morphology of Au film on MoS_2 and SiO_2.

determine the achievable doping concentration.[21] Previous works mainly use dielectric and semiconducting materials as the photon-absorption layer, which usually generate limited number of carriers, and very low doping concentration can be realized by this approach. In addition, the trap states may gradually release the trapped carriers,[25] leading to the decay of doping concentration after removal of photoillumination. Therefore, the photoinduced doping method is rarely applicable due to the doping concentration constraint ($<10^{13}$ cm^{-2}) and stability issue as compared with the conventional doping method, though photoinduced prominent and persistent current based on a similar mechanism has been widely reported on TMDs.[25−28]

Here, we propose a novel photoinduced doping mechanism based on an external photoelectric effect to accomplish a stable and high doping concentration in MoS_2 field-effect transistors (FETs). The device is fabricated by depositing a Au layer (~6 nm) on the channel of the MoS_2 FET and annealing the device in the gas mixture of argon (Ar) and oxygen (O_2) (v/v = 98:2). After annealing, the Au film is well wetted on a MoS_2 channel, which is revealed by both scanning electron microscope (SEM) and atomic force microscope (AFM) measurements. Conductive AFM (CAFM) and X-ray photoelectron spectroscopy (XPS) results further indicate the formation of an oxidation layer (e.g., MoO_3) at the interface. When the fabricated device (shortened as annealed Au/MoS_2 FET) is exposed to ultraviolet (UV) illumination (central wavelength is 254 nm), the Au layer emits electrons due to the external photoelectric effect and becomes positively charged, which in turn induces n-type doping in MoS_2. The doping concentration is calculated to be as high as 10^{14} cm^{-2} upon UV illumination, according to the evolution of the transfer characteristics of the annealed Au/MoS_2 FET. This value is over 1 order of magnitude higher than the previously reported best values by photoinduced doping methods and is comparable to the doping concentration achieved by other conventional methods. Furthermore, the doping level decays only less than 23% after 7 day ambient exposure (non-observable decay in vacuum over 1 day) according to the device resistance monitored in real time. We ascribe those great improvements in doping density and stability to the utilization of metal as the photon-absorption layer, which takes advantage of an external photoelectric effect to induce a higher carrier concentration and eliminate the nonstable charge separation processes. In addition, we have applied the same approach to another two TMDs: ReS_2 and $MoSe_2$, both exhibit a similar photoinduced doping effect. The achieved stable and high-concentration doping on the annealed Au/MX_2 (M is Mo or Re; and X is S or Se) FETs by convenient UV treatment enables various photoelectronic applications such as photoswitch, photomemory,[29−31] and photonic neuromorphic devices.

RESULTS AND DISCUSSION

Figure 1 plots the fabrication procedure of the annealed Au/MoS_2 FET and its resultant morphology characterized by SEM and AFM. Specifically, the bare MoS_2 FET as shown in Figure 1a was fabricated by mechanical exfoliating and transferring a MoS_2 flake from the bulk material to the SiO_2/Si substrate (Si was degenerately doped and covered with 285 nm thick SiO_2) followed by Ti/Au (10/35 nm) electrode deposition. Then, a 6 nm continuous Au film was deposited on MoS_2 (shown in Figure 1b), which was then annealed in the mixture of Ar and O_2 (v/v = 98:2) under 350 °C for 30 min (Supporting Information Figure S1 presents the morphologies and UV responses of annealed Au/MoS_2 FETs deposited with various Au film thicknesses). After annealing, the Au film is well wetted on the MoS_2 surface (the schematic is shown in Figure 1c), the edges of which are re-arranged along the crystallographic orientation of MoS_2, as shown in SEM (Figure 1d,e) and AFM (Figure 1f) images. This wetting phenomenon is in stark contrast with annealing Au film on the SiO_2 substrate, where Au nanoparticles are formed instead of well-wetting morphology.[32] Additionally, we discovered that the Au film shows similar wetting behavior on ReS_2 (Figure 7a), $MoSe_2$ (Supporting Information Figure S12), and WSe_2 (Supporting Information Figure S14) as that on MoS_2, whereas it presents similar dewetting behavior on $MoTe_2$ (Figure 7d) and WTe_2 (Supporting Information Figure S13) as that on SiO_2. The possible reasons for the dewetting behavior in $MoTe_2$ and WTe_2 may be the evaporation of tellurium atoms and

DOI: 10.1021/acsami.8b07196
ACS Appl. Mater. Interfaces 2018, 10, 27840−27849

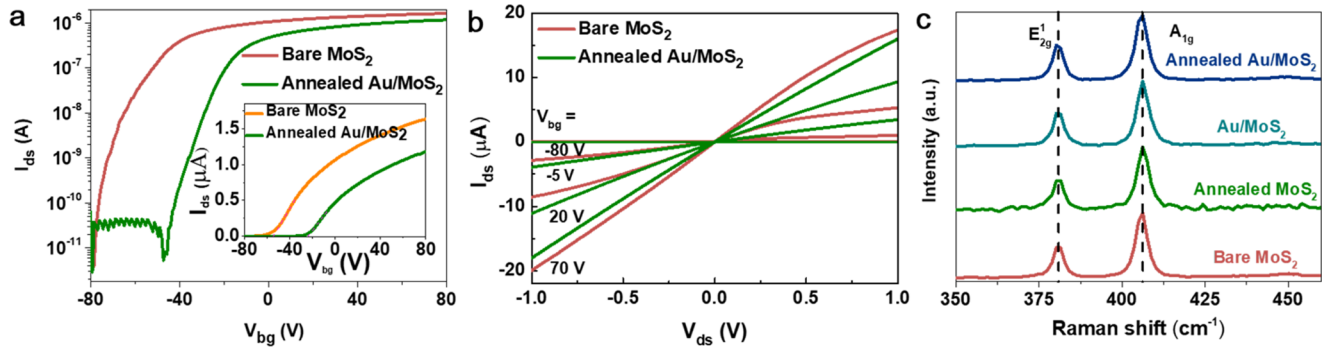

Figure 2. (a) $I_{ds}-V_{bg}$ and (b) $I_{ds}-V_{ds}$ curve evolutions of annealed Au/MoS_2. (c) Raman spectra of bare MoS_2, annealed MoS_2, Au/MoS_2, and annealed Au/MoS_2.

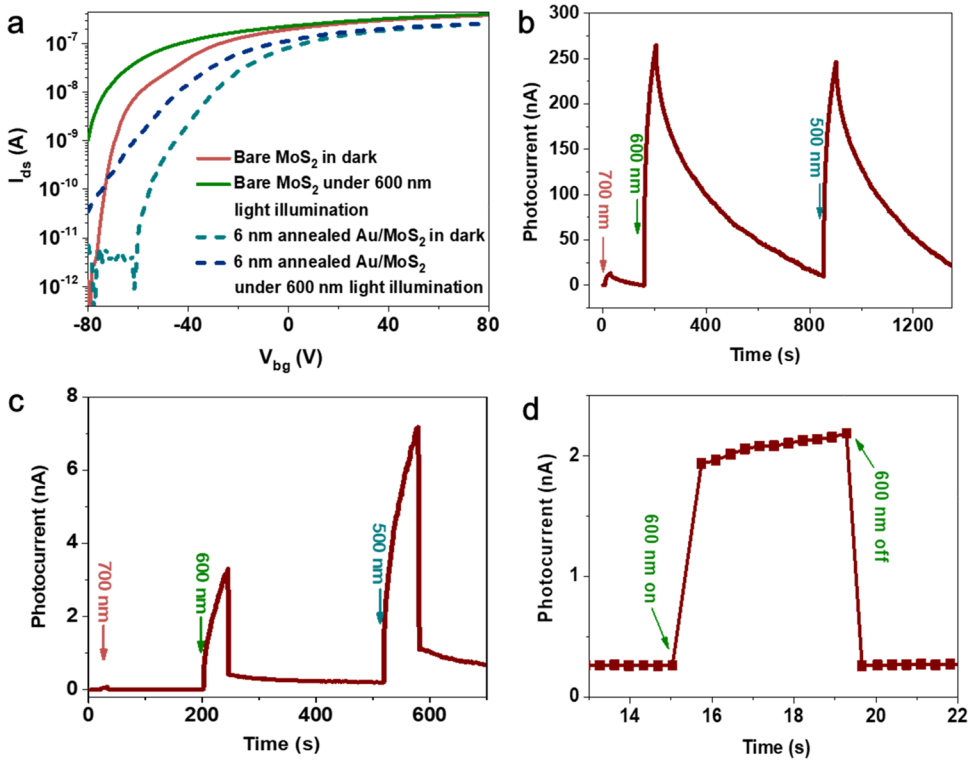

Figure 3. Photoresponses of MoS_2 FET to visible light before and after Au film (6 nm) deposition and annealing. (a) $I_{ds}-V_{bg}$ curves of bare and annealed Au/MoS_2 FETs under dark and 600 nm light. (b, c) Dynamic photoresponses of bare MoS_2 (b) and annealed Au/MoS_2 FET (c) to light with wavelengths of 700, 600, and 500 nm. (d) Dynamic photoresponse of annealed Au/MoS_2 FET to 600 nm light with increased time resolution to 200 ms.

subsequent change of the lattice structure during annealing.[33,34]

Figure 2 presents the influence of Au deposition and annealing on MoS_2 FET through transport measurements. As compared in Figure 2a, the transfer characteristics of bare MoS_2 FET exhibit n-type behavior (orange line in Figure 2a), whereas after Au film deposition and annealing, the doping level decreases, as visualized by the threshold voltage (V_{th}) shifting from −55 to −24 V (green line in Figure 2a). The change of the doping level is possibly due to the charge transfer from Au[18] (Supporting Information Figure S2a) and/or the oxidation of MoS_2[35] (Supporting Information Figure S2b). Besides, the on/off current ratio and carrier mobility also show a slight degradation after Au deposition and annealing. Figure 2b shows the output curves of the device before (orange line)/after (green line) Au film deposition and annealing. The $I-V$ curves show improved linearity but decreased current level after the formation of wetted Au film. The improved linearity of $I-V$ curves indicates an improved Ohmic contact between MoS_2 and electrodes. Figure 2c displays the Raman spectra of a MoS_2 sample, when it was untreated (bare MoS_2), bare annealed (annealed MoS_2), Au-deposited (Au/MoS_2), and Au-deposited and annealed (annealed Au/MoS_2). Two characteristic peaks of E^1_{2g} at 380 cm^{-1} and A_{1g} at 406 cm^{-1} are observed in all samples. The two peaks are separated by 26 cm^{-1}, which indicates that the sample thickness is more than three layers. On the other hand, no obvious shifts[36] are observed for either E^1_{2g} or A_{1g} peak in any treated samples as compared with bare MoS_2 because the change of doping level induced by the Au film is very low here.[37]

In Figure 3, we investigated the response of the annealed Au/MoS_2 FET to visible light as compared to that of bare

DOI: 10.1021/acsami.8b07196
ACS Appl. Mater. Interfaces 2018, 10, 27840−27849

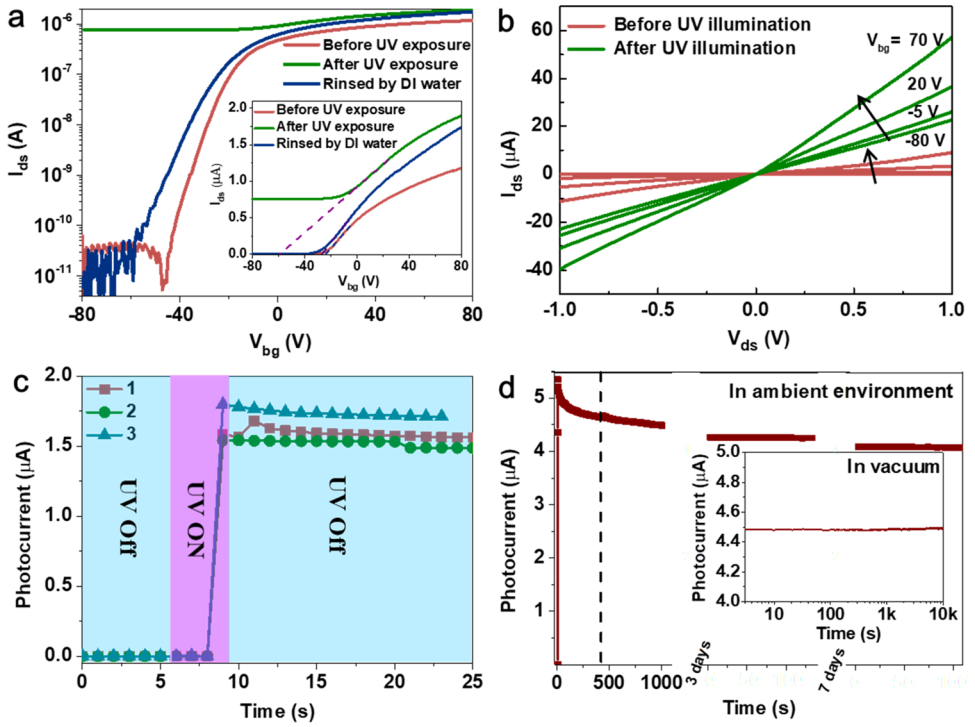

Figure 4. UV-induced photodoping to annealed Au/MoS_2 FET. (a, b) I_{ds}−V_{bg} (a) and I_{ds}−V_{ds} (b) evolution of the device before and after UV illumination and after DI water rinsing. (c) Dynamic UV responses of the device repeated three times. DI water rinsing was applied to recover the device current after UV illumination. (d) Retention time of the device immediately, 3 days, and 7 days after terminating UV illumination in an ambient environment. The inset shows the test in vacuum.

MoS_2 FET. Figure 3a shows the transfer curves of a MoS_2 FET before and after Au deposition and annealing, under dark and 600 nm light illumination, respectively. The threshold voltages of the device before and after Au film deposition and annealing both shift negatively after being exposed under 600 nm light, which corresponds to slightly increased n-type doping after photoillumination. Figure 3b,c shows the dynamic responses of the MoS_2 FET before and after Au deposition and annealing, under 500, 600, and 700 nm light illuminations, respectively. The dynamic photoresponses of both devices can be divided into two steps, which are consistent with the observation reported by previous publications:[38] (1) a fast increase/decrease in channel current immediately after turning on/off the light attributed to the generation and subsequent relaxation of photocarriers, followed by (2) a slow increase/decrease in channel current due to charge trapping at the oxygen-related defect sites on the MoS_2 surface. However, as compared with bare MoS_2 FET, the dynamic response of annealed Au/MoS_2 FET exhibits much faster recovery time (as shown in Figure 3d) but has lower photocurrent. The shortened recovery time after Au deposition and annealing is probably due to the reduction of random local potential fluctuations originated from extrinsic sources, such as gas adsorbates and chemical impurities,[25] by thermal annealing. However, the reduction of photoinduced current is the result of (1) the decline in carrier mobility and on-state current of the device after Au deposition and annealing and (2) the reflections/absorptions of the annealed Au film (the energy of visible light is much smaller than the work function of Au and therefore the increased photocurrent is attributed to the electron−hole pairs generated in MoS_2). Moreover, we observed wavelength-dependent responses for both devices. When the incident photon energy is less than the band gap of MoS_2 (corresponds to 700 nm light illumination), the photocurrent is negligible, whereas the response increases drastically when the incident photon energy exceeds the MoS_2 band gap. A similar phenomenon is also observed in the annealed Au/MoS_2 FETs with different Au film thicknesses (Supporting Information Figures S3 and S4).

We further inspected the photoresponse of annealed Au/MoS_2 FET under UV illumination. For UV illumination, a portable UV lamp was used with the central wavelength at 254 nm and power of 80 μW/cm^2. Figure 4a displays the I_{ds}−V_{bg} curves of the device before (red line) and after (blue line) UV illumination and after deionized (DI) water rinsing (green line). With UV treatment, the annealed Au/MoS_2 FET shows a negative shift in threshold voltage (from −24.00 to −69.48 V) and the off-state current increased by 4 orders of magnitude, based on which we calculate the UV-induced doping concentration to be ~10^{14} cm^{-2}, corresponding to the degenerated n-type doping level. The Hall effect measurement (Supporting Information Figure S5) is also applied to directly identify the doping concentration induced by UV illumination, the result of which is consistent with the concentration calculated on the basis of the transfer curve. Interestingly, the device transfer characteristic can be fully recovered by DI water rinsing, the mechanism of which will be discussed later. The linear output curves of the device after Au deposition and annealing (either before or after UV illumination, Figure 4b) suggest a good Ohmic contact between MoS_2 and electrodes. Moreover, the high channel current level of around 20 μA (V_{bg} = 0 V and V_{ds} = 1 V) indicates that the device is a promising candidate toward UV photoswitch and storage applications. In comparison, bare MoS_2, annealed bare MoS_2, and Au-deposited MoS_2 FETs show weak response to UV light (Supporting Information Figure S6).

DOI: 10.1021/acsami.8b07196
ACS Appl. Mater. Interfaces 2018, 10, 27840−27849

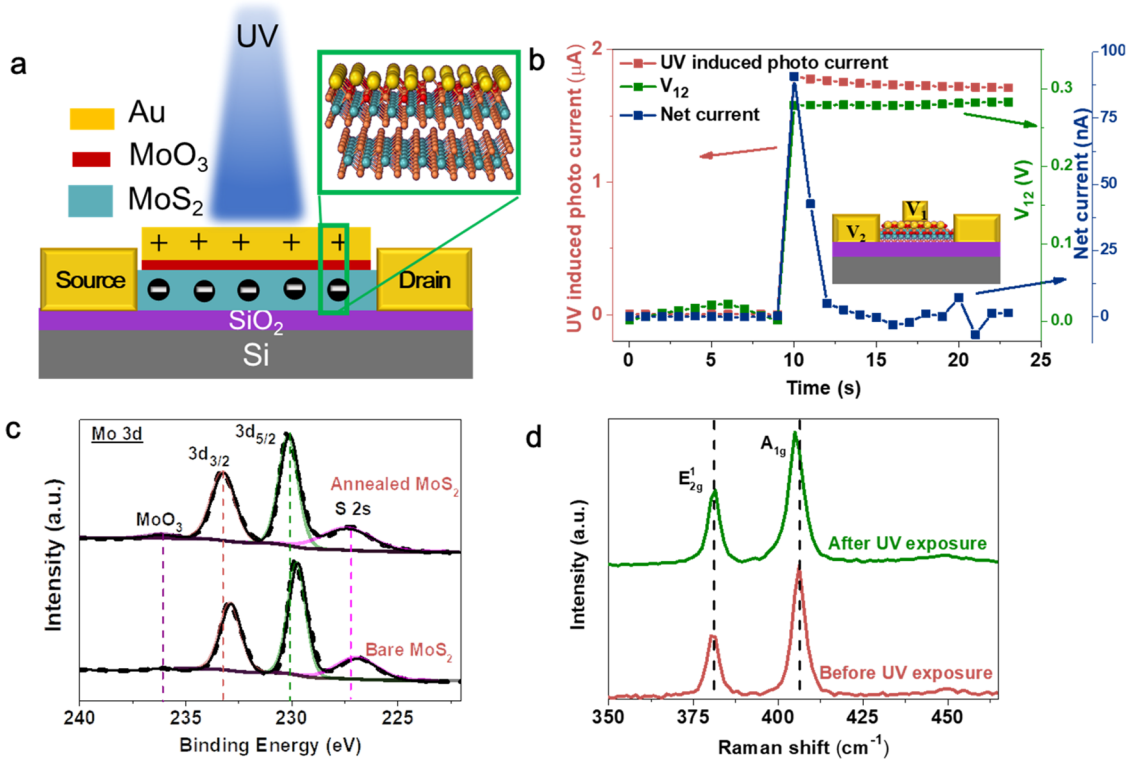

Figure 5. (a) Schematic of the photodoping mechanism. (b) Dynamic current, voltage of V_{12} (V_1−V_2), and net current response upon UV illumination. The inset in (b) shows the schematic of the device. (c) XPS of bare and annealed MoS_2. (d) Raman spectra of the annealed Au/MoS_2 FET before and after UV exposure.

Figure 4c,d shows the dynamic responses of the device to UV illumination when V_{bg} = 0 V and V_{ds} = 0.1 V, respectively. Upon UV illumination, the current increases rapidly from sub-nanoampere to 1.5 μA within 1 s, as shown in Figure 4c. The dynamic variation range of the UV-induced current is comparable to that of a recently reported nonvolatile memory device using a floating-gate structure.[30,31] Additionally, after the removal of UV illumination, the device current does not return to baseline; instead, it stays at the same high level. We then rinsed the device with DI water to recover the signal to the baseline, after which it was exposed to UV light again. As we repeated the above processes over and over again, the device current always increased to 1.5 μA upon UV illumination and remained at this current level after the UV light was turned off. In Figure 4d, we test the retention times of this phenomenon in both ambient and vacuum environments (inset of Figure 4d). In both tests, the device was exposed to UV only at the beginning of the tests and kept in the dark during the entire sequential measurement. In the ambient environment test, the channel current of the device was measured for a time interval of 1000 s, immediately, 3 days, and 7 days after UV light was turned off, respectively. Between each test, the device was stored in the dark and disconnected from any source meters and wires. After 7 days, the total drop of channel current is around 23% (5.3−4.07 μA), over half (16%) of which is contributed by the first 1000 s immediately after the removal of UV illumination. Further analysis reveals that the decay curve can be fitted by a two-exponential decay function[31] with two characteristic decay time constants

$$I_d = A_1 e^{t/\tau_1} + A_2 e^{t/\tau_2}$$

where τ_1 and τ_2 are fitted to be 1.95 × 10^2 and 2.19 × 10^4 s, respectively. The first process (τ_1) contributes 13% of the total current drop and is strongly suppressed after 400 s. The second process (τ_2) dominates the rest of the decay process over 10^4 s. In contrast, the device measured in vacuum (10^{-4} torr, inset of Figure 4d) does not show any obvious current decay for 27 h.

Figure 5a illustrates the potential mechanism of UV-induced doping in annealed Au/MoS_2 FET, which is attributed to the external photoelectric effect upon UV illumination on the Au film. Specifically, under 254 nm (4.88 eV) UV irradiation, the high-energy photons cause emission of high-energy electrons in the wetted Au film. As a result, the Au film becomes positively charged and induces n-type carriers in MoS_2 with the formation of the oxidation layer (e.g., MoO_3) during annealing, which serves as a dielectric layer at the interface between wetted Au film and MoS_2. When the UV light is turned off, the low-energy carriers in MoS_2 cannot move back to Au due to the existence of the oxidation layer at the interface. As a result, the Au film remains positively charged and thus induces persistent n-type doping in MoS_2. According to the external photoelectric effect, this persistent doping effect happens only when the incident photon energy is equal to or higher than the threshold energy to free electrons from wetted Au film, which is consistent with the experimental result that the photo-induced doping is not persistent under visible light illuminations. We rule out the possibility that the persistent UV-induced doping is caused by the phase shift of annealed Au/MoS_2 from a 2H to a 1T phase after UV illumination by Raman spectroscopy and temperature-dependent transport measurements (Supporting Information Figure S7).

To test the hypothesis, we have added an additional top electrode on the wetted Au film to monitor the potential

DOI: 10.1021/acsami.8b07196
ACS Appl. Mater. Interfaces 2018, 10, 27840−27849

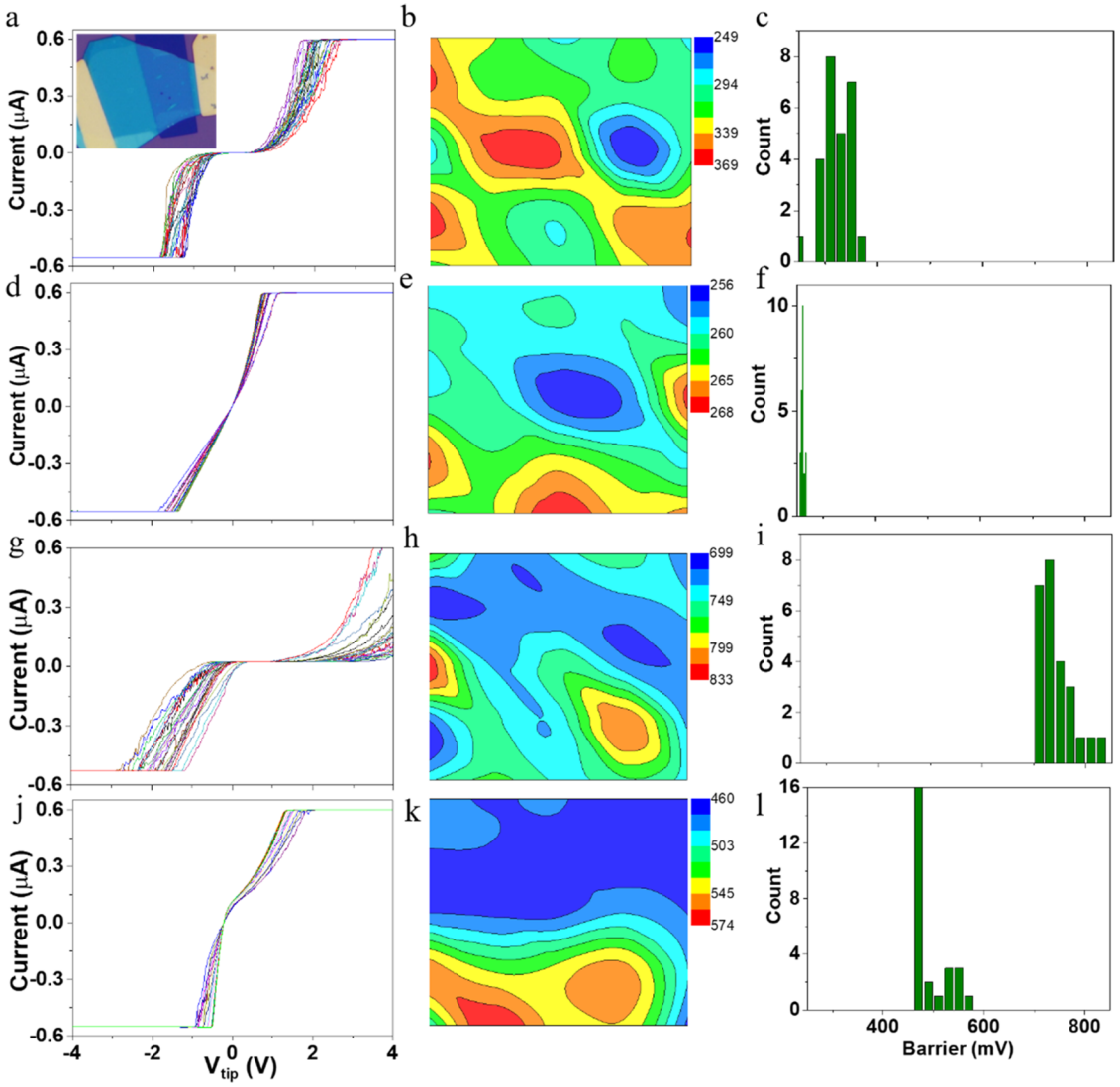

Figure 6. Current-voltage curves (I–V_{tip}) measured by CAFM on bare (a), Au-coated (d), annealed bare (g), and annealed Au-coated (j) MoS_2. The upper-left inset in (a) shows the optical image of the device for CAFM measurement, and half of the MoS_2 channel is coated with the Au film. Two-dimensional maps (b, e, h, k) and histograms (c, f, i, l) of the SBHs extracted from linear fitting of I–V_{tip} in (a), (d), (g), (j), respectively.

change of the wetted Au film (inset of Figure 5b). As shown in Figure 5b, the potential difference V_{12} between the top and source electrodes (grounded) changes from 0 to ∼+280 mV (green line) when the device is exposed to UV illumination and remains at this value after the UV light is turned off. Simultaneously, we have observed an increase in the channel current (red line) as V_{12} increases. We then grounded the top electrode to release the charges carried by Au, which immediately leads to the significant decrease of the channel current (Supporting Information Figure S8). Moreover, we measured the difference of the work function between the annealed bare MoS_2 and annealed Au/MoS_2 regions in the same MoS_2 flake by a Kelvin probe force microscope (KPFM). As compared to the difference before UV illumination, the difference of the work function between these two regions changed around 400 mV after UV exposure, as presented in Supporting Information Figure S9. These observations verify that the wetted Au film is persistently charged after UV illumination, which contributes to the persistent high channel current. We further calculated the net current flowing into the MoS_2 channel from the three electrodes of source, drain, and back gate ($I_{net} = I_{drain} + I_{source} + I_{bg}$) by measuring the current flowing into (+) and out of (−) the channel from each electrode. As shown by a blue line in Figure 5b, the I_{net} increases immediately from picoampere to around +90 nA when the device is exposed to UV and returns to pA within 5 s. The increase of net current from pA to +90 nA indicates a negative net current (or net electrons) injecting into MoS_2 from the top electrode. We then estimated the sheet doping concentration of MoS_2 based on the change of net current using the following formula

$$D_{2n} = \frac{n}{A} = \frac{Q}{qA} = \frac{\int I_{net}\,dt}{qA}$$

where D_{2n} is the sheet doping concentration, n is the number of electrons, A is the area of channel, Q is the net total charge, and q is the electron charge. The calculated sheet doping concentration is around 10^{14} cm^{-2}, which is at the same level as the value calculated from the transfer curve. Raman spectroscopy was also applied to investigate the UV-induced doping effect as a large doping density can shift the A_{1g} mode.

DOI: 10.1021/acsami.8b07196
ACS Appl. Mater. Interfaces 2018, 10, 27840−27849

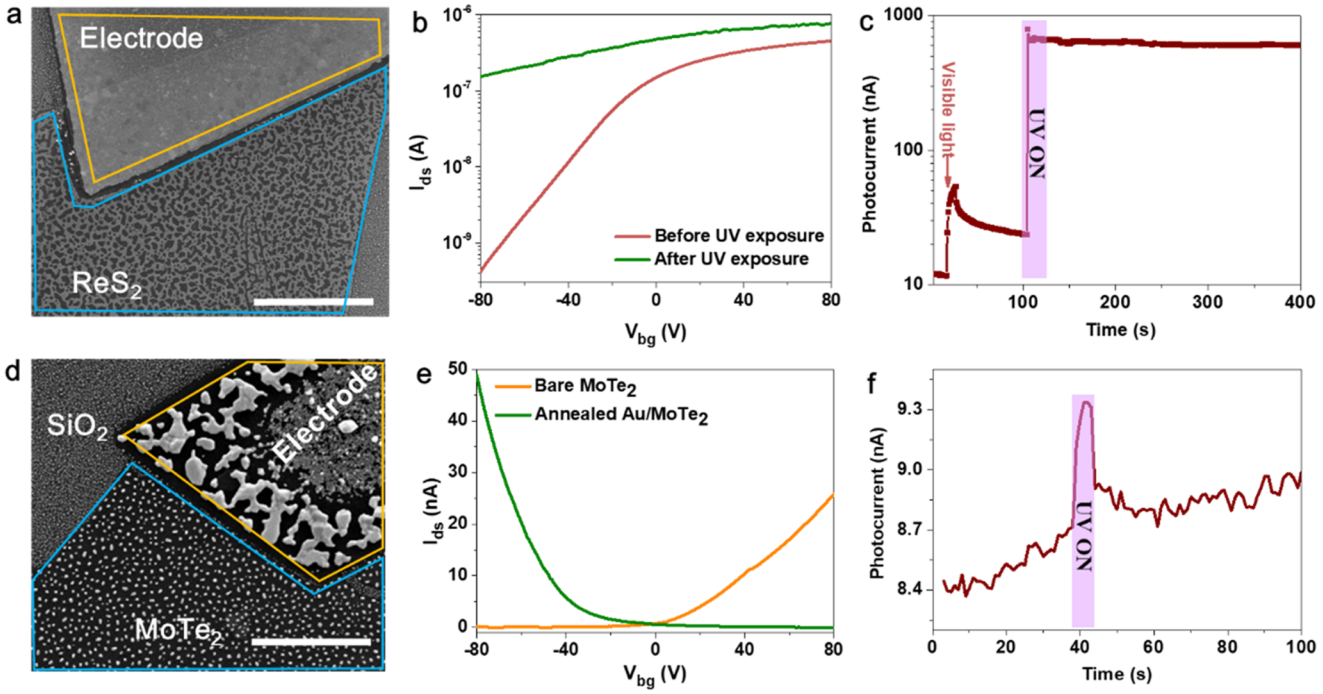

Figure 7. (a) SEM image (scale bar is 5 μm) of Au film morphology on ReS_2 after annealing. (b) Evolution of $I_{ds}-V_{bg}$ curves of annealed Au/ReS_2 FET before and after UV illumination. (c) Dynamic response of annealed Au/ReS_2 FET under visible and UV illumination. (d) SEM image (scale bar is 20 μm) of Au film morphology on $MoTe_2$ after annealing. (e) Evolution of $I_{ds}-V_{bg}$ curves of $MoTe_2$ FET before and after Au decoration and annealing. (f) Dynamic response of the annealed Au/$MoTe_2$ FET under UV illumination.

As shown in Figure 5d, the A_{1g} mode downshifts by 2 cm^{-1} after UV radiation, which is consistent with a previous report that the high electron concentration can soften the vibration of A_{1g}.[6]

The existence of the dielectric layer is experimentally verified by XPS and CAFM measurements. Figure 5d compares the XPS spectra of the Mo element in bare and annealed MoS_2 samples. A peak centered at 236.1 eV is observed in the annealed MoS_2 sample corresponding to the formation of MoO_3. We also took the XPS measurements on the Au-deposited MoS_2 sample before and after annealing, as presented in Supporting Information Figure S10. Due to the existence of Au film, the XPS spectra of the Mo element are too weak to be observed. However, the XPS characteristic peaks of Au on MoS_2 before annealing shift 0.4 eV compared to those of metallic Au^0 due to the formation of the S−Au bond, whereas after annealing, the peaks shift back to the original position, as a result of the separation between the wetted Au film and MoS_2 by the oxidation layer.

We further carried out CAFM measurements. The sample preparation and measurement processes are described in detail in the Experimental Section. According to a previous report,[39] the total resistance contributing to the measured current mainly includes the tip/sample contact resistance and the spreading resistance in the sample region around the tip. It offers the possibility to monitor the Schottky barrier height (SBH) between the tip and sample by means of an $I-V_{tip}$ scan. We first performed the measurement on a MoS_2 flake, half of which was coated with a layer of Au. A series of $I-V_{tip}$ curves were collected from the bare MoS_2 (Figure 6a) and Au/MoS_2 (Figure 6d) regions, respectively, by measuring a 5 × 5 array with 50 nm spacing between each point in each region. The spatial distribution of the SBH corresponding to the two samples was calculated by fitting the $I-V_{tip}$ curves, which are presented in Figure 6b,e. The SBHs for both regions lie in the range of 250−350 mV, which is consistent with a previous report.[40] In addition, the average value and distribution range of the SBH for the Au/MoS_2 region are both reduced as compared to those for the bare MoS_2 region. It may be attributed to the fact that Au coating on MoS_2 reduces the contact resistance between the tip and MoS_2. We then thermal-annealed the sample in the mixture of Ar and O_2 (v/v = 98:2). After annealing, the $I-V_{tip}$ curves obtained from both bare MoS_2 and Au/MoS_2 regions display an increased Schottky contact under the forward bias, which are presented in Figure 6g,j, respectively. These asymmetric $I-V_{tip}$ curves indicate the existence of a local Schottky diode between the tip and sample,[39,40] which is likely due to the formation of an oxidized layer at the surface of MoS_2. The SBHs for the annealed bare MoS_2 and annealed Au/MoS_2 regions under the forward bias are collected in Figure 6h,k, which increase from 700 to 830 and 466 to 563 mV, respectively. It further indicates the increase of Schottky barrier between the tip and sample and thus the generation of the oxidation layer. It is to be noted that the oxidation layer on top of MoS_2 induces negligible p-type doping to our device, which is distinct from the previous reports that the oxidation of MoS_2 by soft plasma treatment can p-dope the material.[40,35] This may be because in our case the regions covered by the source and drain electrodes are not oxidized and the exposed regions are only oxidized by few top layers.

Finally, we fabricated the Au/oxidation layer/MoS_2 structure by physically depositing the oxidation layer of MoO_3 (and Al_2O_3) on the MoS_2 flake. As shown in Supporting Information Figure S11, the same UV responses are observed in this configuration as in the annealed Au/MoS_2 device, when the thickness of the MoO_3 (and Al_2O_3) layer achieves 4 nm (and 2 nm). It not only indicates the existence of the oxidation

DOI: 10.1021/acsami.8b07196
ACS Appl. Mater. Interfaces 2018, 10, 27840−27849

layer in the annealed Au/MoS_2 device but also supports the proposed mechanism for the UV-induced photocurrent.

The proposed photoinduced doping mechanism can also explain the channel current retention behavior and rapid discharge process after DI water rinsing. The retention behavior of the device is because of the fact that the discharge process of the Au film is slow under ambient conditions without efficient discharge channels. On the other hand, the channel current immediately decreases to the baseline after DI water rinsing because DI water is conductive so that it shorts the wetted Au film and MoS_2 channel (in a control experiment, isopropanol alcohol rinsing cannot recover the device transfer characteristic). Consequently, capping the Au film from the ambient environment may greatly enhance the doping stability.

Finally, we investigated the UV-induced doping effect on other TMD FETs modified by the same procedure to explore its versatility. Figure 7a shows the SEM image of Au-deposited ReS_2 FETs after annealing, in which the same wetting morphology of the Au film as that on MoS_2 is observed. Its transfer characteristic also exhibits significantly increased off-state current after UV illumination, indicating increased n-type doping in ReS_2 (Figure 7b). In Figure 7c, the dynamic responses of the device to visible and UV light are presented. The results indicate that the doping induced by the UV light is persistent and more than 10 times higher than that induced by visible light. A similar behavior is also observed in the annealed Au/$MoSe_2$ FET (Supporting Information Figure S12). In contrast, Figure 7d shows the SEM image of the Au-deposited $MoTe_2$ FET after annealing, in which the Au film forms Au nanoparticles instead of wetting on $MoTe_2$. Additionally, the device switches from n-type to p-type after Au deposition (as shown in Figure 7e), which is consistent with the previous report.[41] The UV illumination induces only very limited p-type doping to the device, and the doping level decays rapidly after the removal of UV illumination (Figure 7f). The same morphology, transfer characteristic, and UV response are observed for the annealed Au/WTe_2 FET (Supporting Information Figure S13). The photoinduced doping effect observed in annealed Au/MoS_2, $MoSe_2$, and ReS_2 FETs may be due to the fact that Re and Mo can be oxidized and form a dielectric layer at the interface between the conduction and wetted Au layers during the annealing process, whereas the $MoTe_2$ and WTe_2 FETs form Au nanoparticles instead of wetting morphology of Au film after annealing. Table 1 lists the conduction types of bare TMD FETs and Au-deposited TMD FETs after annealing, Au film wetting morphologies after annealing, and their UV responses. From this table, a rough law can be drawn that the TMDs comprising Mo/Re and S/Se molecules are likely to have UV-induced doping effect, whereas the TMDs with Te molecules do not have such phenomenon.

Table 1. Summary of Conduction Types, Au Film Morphologies after Annealing, and UV-Induced Doping of TMDs

TMDs	bare	Au deposition and annealing	Au morphology	UV-induced doping
MoS_2	n type	n type	wetting	persistent
ReS_2	n type	n type	wetting	persistent
$MoSe_2$	n type	n type	wetting	persistent
WSe_2	n type	p type	wetting	negligible
$MoTe_2$	n type	p type	dewetting	negligible
WTe_2	n type	p type	dewetting	negligible

An exception to this law is WSe_2, on which Au exhibits wetting morphology, but the device does not show the UV-induced doping effect (Supporting Information Figure S14). This anomaly may be because of the fact that the device becomes p-type after Au deposition and annealing, which is then tuned to off-state by the UV-induced positive bias on the Au film. As a result, it shows a limited UV response.

CONCLUSIONS

In conclusion, we have demonstrated a novel photoinduced doping approach based on the external photoelectric effect to achieve a stable and high-concentration doping for layered MX_2 (M is Mo or Re, and X is S or Se). By sequentially depositing and annealing the Au layer on the surface, the MX_2 becomes n-type-doped after UV illumination. The doping can reach a degenerated concentration level of around 10^{14} cm^{-2} and exhibits long-term stability. The doping is also reversible by grounding the top Au film. Two key factors are found to account for this doping mechanism by performing comparison experiments: the wetting behavior of the Au film and formation of a dielectric layer at the Au−MX_2 interface during the annealing process. This convenient photodoping approach potentially enables many possibilities toward fantastic photo-controllable electronic devices.

EXPERIMENTAL SECTION

Device Fabrication. The 2H-MoS_2 flake was mechanically exfoliated by tape from the bulk crystal and transferred onto a SiO_2/Si substrate (SiO_2 layer was 285 nm thick). The source and drain electrodes were defined on the MoS_2 flake using e-beam lithography (EBL) with a double-layer resist recipe. Ti and Au films were then sequentially deposited on the flake through e-beam evaporation with thicknesses of 10 and 35 nm, respectively, forming a Ti/Au contact, which was followed by a standard lift-off process to complete the fabrication of bare MoS_2 FET. To fabricate Au-deposited MoS_2 FET, an area located at the center of the MoS_2 flake was patterned for additional Au film deposition by EBL with a gap of sub-micron to each electrode. The additional layer of Au was deposited by e-beam evaporation at a fixed rate of 0.2 Å/s. After Au deposition, the device was annealed in a tube furnace filled with a gas mixture of O_2 (2%) and Ar (98%) to form annealed Au/MoS_2 FET. During annealing, the temperature of the furnace was first increased from room temperature to 350 °C at a rate of 10 °C/min and then the furnace was kept at this temperature for 30 min, which was then cooled down to room temperature naturally. The annealed bare MoS_2 FET was fabricated by the same recipe as that used for annealed Au/MoS_2 FET except that it was not deposited with an additional layer of Au film on the surface. The sample for CAFM measurements was prepared by transferring a MoS_2 flake onto the SiO_2/Si substrate, followed by depositing two Ti (10 nm)/Au (35 nm) contacts using the EBL process. After electrode deposition, half of the MoS_2 flake was deposited with 6 nm Au film.

Sample Characterization. AFM characterization was conducted by Dimension Icon (Bruker, German) in the tapping mode. Raman spectra were obtained from a Renishaw InVia Raman microscope with ~1.38 mW excitation at 532 nm. XPS measurements were performed in ultrahigh vacuum by ESCALAB 250 Xi (Thermo Scientific) with a nominal spot size of 400 μm. The binding energies obtained in the spectral analysis were corrected by referencing C 1s to 284.6 eV. The electrical characteristics of MoS_2 devices were inspected by semiconductor parameter analyzer B1500 (Agilent) in ambient conditions. All of the I_{ds}−V_{bg} curves were obtained under a 0.05 V source−drain bias, if not specially noted. The time resolution result was obtained under a 0.1 V source−drain bias and 0 V gate bias.

For CAFM measurements, a Pt-coated AFM tip with a 30 nm contact radius was used to scan the I−V_{tip} curves. The voltage bias was applied on the tip, whereas the two electrodes deposited on MoS_2

DOI: 10.1021/acsami.8b07196
ACS Appl. Mater. Interfaces 2018, 10, 27840−27849

were electrically grounded. The current flowing through the MoS_2 film was recorded by a current sensor. The local $I-V_{tip}$ characteristics obtained from CAFM measurements follow the thermionic emission equation

$$I = A_{tip}A^*T^2 \exp\left(-\frac{q\varnothing_B}{\kappa T}\right)\exp\left(-\frac{qV_{tip}}{n\kappa T}\right)$$

where $A_{tip} = \pi r^2$ is the tip contact area, A^* is the Richardson constant, $T = 300$ K, $\varnothing_B$ is the Schottky barrier, κ is the Boltzmann constant, q is the electron charge, and n is the idea factor. By linear fitting the semi-log $I-V_{tip}$ curve, the SBH and n can be calculated by the intercept and slope.

Carrier mobility was calculated using the following equation

$$\mu = \frac{L}{WC_{ox}V_{ds}}\frac{dI_{ds}}{dV_{bg}}$$

and the total carrier concentration of the device was extracted by the formula

$$n_{2D} = \frac{I_{ds}L}{qWV_{ds}\mu}$$

where μ is the carrier mobility, L and W are the channel length and width, respectively, as measured by SEM, $\frac{dI_{ds}}{dV_{bg}}$ is the transconductance, C_{ox} is the gate oxide capacitance of 11 nF/cm^2 for 285 nm thick dry thermal SiO_2, and V_{ds} is the source−drain voltage.

■ ASSOCIATED CONTENT

Supporting Information

The Supporting Information is available free of charge on the ACS Publications website at DOI: 10.1021/acsami.8b07196.

SEM images and UV responses of annealed Au/MoS_2 devices with different Au film thicknesses, evolution of transfer characteristics of the devices during fabrication, visible light response of bare MoS_2 and annealed Au/MoS_2 devices, Hall effect measurement, dynamic UV current of different devices, investigation of MoS_2 phase transition, recovery of UV-induced photocurrent, KPFM measurement, XPS measurement, UV response of the Au/oxidation layer/MoS_2 structure, and characterization of annealed Au/MX_2 (PDF)

■ AUTHOR INFORMATION

Corresponding Author

*E-mail: jingliu_1112@tju.edu.cn.

ORCID

Qiankun Zhang: 0000-0003-4339-4348
Daihua Zhang: 0000-0002-0163-0616
Dong Sun: 0000-0002-0898-4548
Jing Liu: 0000-0002-8993-4074

Notes

The authors declare no competing financial interest.

■ ACKNOWLEDGMENTS

This project has been supported by the National Science Foundation of China (NSFC Grant No. 21405109) and Seed Foundation of State Key Laboratory of Precision Measurement Technology and Instruments (Pilt No. 1710).

■ REFERENCES

(1) Zhao, Y.; Xu, K.; Pan, F.; Zhou, C.; Zhou, F.; Chai, Y. Doping, Contact and Interface Engineering of Two-Dimensional Layered Transition Metal Dichalcogenides Transistors. *Adv. Funct. Mater.* **2017**, *27*, No. 1603484.

(2) Bhimanapati, G. R.; Lin, Z.; Meunier, V.; Jung, Y.; Cha, J.; Das, S.; Xiao, D.; Son, Y.; Strano, M. S.; Cooper, V. R.; Liang, L.; Louie, S. G.; Ring, E.; Zhou, W.; Kim, S. S.; Naik, R. R.; Sumpter, B. G.; Terrones, H.; Xia, F.; Wang, Y.; Zhu, J.; Akinwande, D.; Alem, N.; Schuller, J. A.; Schaak, R. E.; Terrones, M.; Robinson, J. A. Recent Advances in Two-Dimensional Materials beyond Graphene. *ACS Nano* **2015**, *9*, 11509−11539.

(3) Hu, Z.; Wu, Z.; Han, C.; He, J.; Ni, Z.; Chen, W. Two-Dimensional Transition Metal Dichalcogenides: Interface and Defect Engineering. *Chem. Soc. Rev.* **2018**, *47*, 3100−3128.

(4) Di, J.; Xiong, J.; Li, H.; Liu, Z. Ultrathin 2D Photocatalysts: Electronic-Structure Tailoring, Hybridization, and Applications. *Adv. Mater.* **2018**, *30*, 1−30.

(5) Saran, R.; Curry, R. J. Lead Sulphide Nanocrystal Photodetector Technologies. *Nat. Photonics* **2016**, *10*, 81−92.

(6) Kiriya, D.; Tosun, M.; Zhao, P.; Kang, J. S.; Javey, A. Air-Stable Surface Charge Transfer Doping of MoS_2 by Benzyl Viologen. *J. Am. Chem. Soc.* **2014**, *136*, 7853−7856.

(7) Geim, A. K.; Grigorieva, I. V. Van Der Waals Heterostructures. *Nature* **2013**, *499*, 419−425.

(8) Duan, X.; Wang, C.; Fan, Z.; Hao, G.; Kou, L.; Halim, U.; Li, H.; Wu, X.; Wang, Y.; Jiang, J.; Pan, A.; Huang, Y.; Yu, R.; Duan, X. Synthesis of WS_{2X} Se_{2-2X} Alloy Nanosheets with Composition-Tunable Electronic Properties. *Nano Lett.* **2016**, *16*, 264−269.

(9) Gong, Y.; Liu, Z.; Lupini, A. R.; Shi, G.; Lin, J.; Najmaei, S.; Lin, Z.; Elías, A. L.; Berkdemir, A.; You, G.; Terrones, H.; Terrones, M.; Vajtai, R.; Pantelides, S. T.; Pennycook, S. J.; Lou, W.; Ajayan, P. M.; Zhou, W. Band Gap Engineering and Layer-by-Layer Mapping of Selenium-Doped Molybdenum Disulfide. *Nano Lett.* **2014**, *14*, 442−449.

(10) Dolui, K.; Rungger, I.; Das Pemmaraju, C.; Sanvito, S. Possible Doping Strategies for MoS_2 Monolayers: An Ab Initio Study. *Phys. Rev. B* **2013**, *88*, 1−9.

(11) Lin, Y. C.; Dumcenco, D. O.; Huang, Y. S.; Suenaga, K. Atomic Mechanism of the Semiconducting-to-Metallic Phase Transition in Single-Layered MoS_2. *Nat. Nanotechnol.* **2014**, *9*, 391−396.

(12) Åhlgren, E. H.; Kotakoski, J.; Krasheninnikov, A. V. Atomistic Simulations of the Implantation of Low-Energy Boron and Nitrogen Ions into Graphene. *Phys. Rev. B* **2011**, *83*, 1−7.

(13) Chen, M.; Nam, H.; Wi, S.; Ji, L.; Ren, X.; Bian, L.; Lu, S.; Liang, X. Stable Few-Layer MoS_2 rectifying Diodes Formed by Plasma-Assisted Doping. *Appl. Phys. Lett.* **2013**, *103*, No. 142110.

(14) Nipane, A.; Karmakar, D.; Kaushik, N.; Karande, S.; Lodha, S. Few-Layer MoS_2 p-Type Devices Enabled by Selective Doping Using Low Energy Phosphorus Implantation. *ACS Nano* **2016**, *10*, 2128−2137.

(15) Tongay, S.; Zhou, J.; Ataca, C.; Liu, J.; Kang, J. S.; Matthews, T. S.; You, L.; Li, J.; Grossman, J. C.; Wu, J. Broad-Range Modulation of Light Emission in Two-Dimensional Semiconductors by Molecular Physisorption Gating. *Nano Lett.* **2013**, *13*, 2831−2836.

(16) Huo, N.; Yang, S.; Wei, Z.; Li, S.-S.; Xia, J.-B.; Li, J. Photoresponsive and Gas Sensing Field-Effect Transistors Based on Multilayer WS_2 Nanoflakes. *Sci. Rep.* **2015**, *4*, No. 5209.

(17) Liu, X.; Qu, D.; Ryu, J.; Ahmed, F.; Yang, Z.; Lee, D.; Yoo, W. J. P-Type Polar Transition of Chemically Doped Multilayer MoS_2 Transistor. *Adv. Mater.* **2016**, *28*, 2345−2351.

(18) Sarkar, D.; Xie, X.; Kang, J.; Zhang, H.; Liu, W.; Navarrete, J.; Moskovits, M.; Banerjee, K. Functionalization of Transition Metal Dichalcogenides with Metallic Nanoparticles: Implications for Doping and Gas-Sensing. *Nano Lett.* **2015**, *15*, 2852−2862.

(19) Andleeb, S.; Kumar Singh, A.; Eom, J. Chemical Doping of MoS_2 Multilayer by P-Toluene Sulfonic Acid. *Sci. Technol. Adv. Mater.* **2015**, *16*, No. 035009.

(20) Fang, H.; Tosun, M.; Seol, G.; Chang, T. C.; Takei, K.; Guo, J.; Javey, A. Degenerate N-Doping of Few-Layer Transition Metal Dichalcogenides by Potassium. *Nano Lett.* **2013**, *13*, 1991−1995.

DOI: 10.1021/acsami.8b07196
ACS Appl. Mater. Interfaces 2018, 10, 27840−27849

(21) Ho, P. H.; Chen, C. H.; Shih, F. Y.; Chang, Y. R.; Li, S. S.; Wang, W. H.; Shih, M. C.; Chen, W. T.; Chiu, Y. P.; Li, M. K.; Shih, Y. S.; Chen, C. W. Precisely Controlled Ultrastrong Photoinduced Doping at Graphene-Heterostructures Assisted by Trap-State-Mediated Charge Transfer. *Adv. Mater.* **2015**, *27*, 7809−7815.
(22) Wang, X. H.; Ning, J. Q.; Su, Z. C.; Zheng, C. C.; Zhu, B. R.; Xie, L.; Wu, H. S.; Xu, S. J. Photoinduced Doping and Photoluminescence Signature in an Exfoliated WS_2 Monolayer Semiconductor. *RSC Adv.* **2016**, *6*, 27677−27681.
(23) Martinez, I.; Ribeiro, M.; Andres, P.; Hueso, L. E.; Casanova, F.; Aliev, F. G. Photodoping-Driven Crossover in the Low-Frequency Noise of MoS_2 Transistors. *Phys. Rev. Appl.* **2017**, *7*, 1−8.
(24) Ju, L.; Velasco, J.; Huang, E.; Kahn, S.; Nosiglia, C.; Tsai, H. Z.; Yang, W.; Taniguchi, T.; Watanabe, K.; Zhang, Y.; Zhang, G.; Crommie, M.; Zettl, A.; Wang, F. Photoinduced Doping in Heterostructures of Graphene and Boron Nitride. *Nat. Nanotechnol.* **2014**, *9*, 348−352.
(25) Wu, Y. C.; Liu, C. H.; Chen, S. Y.; Shih, F. Y.; Ho, P. H.; Chen, C. W.; Liang, C. T.; Wang, W. H. Extrinsic Origin of Persistent Photoconductivity in Monolayer MoS_2 Field Effect Transistors. *Sci. Rep.* **2015**, *5*, No. 11472.
(26) Singh, A. K.; Andleeb, S.; Singh, J.; Dung, H. T.; Seo, Y.; Eom, J. Ultraviolet-Light-Induced Reversible and Stable Carrier Modulation in MoS_2 Field-Effect Transistors. *Adv. Funct. Mater.* **2014**, *24*, 7125−7132.
(27) Liu, F.; Zhu, C.; You, L.; Liang, S. J.; Zheng, S.; Zhou, J.; Fu, Q.; He, Y.; Zeng, Q.; Fan, H. J.; Ang, L. K.; Wang, J.; Liu, Z. 2D Black Phosphorus/$SrTiO_3$-Based Programmable Photoconductive Switch. *Adv. Mater.* **2016**, *28*, 7768−7773.
(28) Roy, K.; Padmanabhan, M.; Goswami, S.; Sai, T. P.; Ramalingam, G.; Raghavan, S.; Ghosh, A. Graphene-MoS_2 Hybrid Structures for Multifunctional Photoresponsive Memory Devices. *Nat. Nanotechnol.* **2013**, *8*, 826−830.
(29) Lee, D.; Hwang, E.; Lee, Y.; Choi, Y.; Kim, J. S.; Lee, S.; Cho, J. H. Multibit MoS_2 Photoelectronic Memory with Ultrahigh Sensitivity. *Adv. Mater.* **2016**, *28*, 9196−9202.
(30) Li, D.; Wang, X.; Zhang, Q.; Zou, L.; Xu, X.; Zhang, Z. Nonvolatile Floating-Gate Memories Based on Stacked Black Phosphorus-Boron Nitride-MoS_2 heterostructures. *Adv. Funct. Mater.* **2015**, *25*, 7360−7365.
(31) Lee, J.; Pak, S.; Lee, Y.-W.; Cho, Y.; Hong, J.; Giraud, P.; Shin, H. S.; Morris, S. M.; Sohn, J. I.; Cha, S.; Kim, J. M. Monolayer Optical Memory Cells Based on Artificial Trap-Mediated Charge Storage and Release. *Nat. Commun.* **2017**, *8*, No. 14734.
(32) Thompson, C. V. Solid-State Dewetting of Thin Films. *Annu. Rev. Mater. Res.* **2012**, *42*, 399−434.
(33) Diaz, H. C.; Chaghi, R.; Ma, Y.; Batzill, M. Molecular Beam Epitaxy of the van Der Waals Heterostructure $MoTe_2$ on MoS_2: Phase, Thermal, and Chemical Stability. *2D Mater.* **2015**, *2*, No. 044010.
(34) Ueno, K.; Fukushima, K. Changes in Structure and Chemical Composition of α-$MoTe_2$ and β-$MoTe_2$ during Heating in Vacuum Conditions. *Appl. Phys. Express* **2015**, *8*, No. 095201.
(35) Zhu, H.; Qin, X.; Cheng, L.; Azcatl, A.; Kim, J.; Wallace, R. M. Remote Plasma Oxidation and Atomic Layer Etching of MoS_2. *ACS Appl. Mater. Interfaces* **2016**, *8*, 19119−19126.
(36) Sreeprasad, T. S.; Nguyen, P.; Kim, N.; Berry, V. Controlled, Defect-Guided, Metal-Nanoparticle-Incorporation onto MoS_2 via Chemical and Microwave Routes: Electrical, Thermal, and Structural Properties. *Nano Lett.* **2013**, *13*, 4434−4441.
(37) Xu, K.; Wang, Y.; Zhao, Y.; Chai, Y. Modulation Doping of Transition Metal Dichalcogenide/oxide Heterostructures. *J. Mater. Chem. C* **2017**, *5*, 376−381.
(38) Lopez-Sanchez, O.; Lembke, D.; Kayci, M.; Radenovic, A.; Kis, A. Ultrasensitive Photodetectors Based on Monolayer MoS_2. *Nat. Nanotechnol.* **2013**, *8*, 497−501.
(39) Giannazzo, F.; Fisichella, G.; Piazza, A.; Agnello, S.; Roccaforte, F. Nanoscale Inhomogeneity of the Schottky Barrier and Resistivity in MoS2 Multilayers. *Phys. Rev. B* **2015**, *92*, 1−4.
(40) Giannazzo, F.; Fisichella, G.; Greco, G.; Di Franco, S.; Deretzis, I.; La Magna, A.; Bongiorno, C.; Nicotra, G.; Spinella, C.; Scopelliti, M.; Pignataro, B.; Agnello, S.; Roccaforte, F. Ambipolar MoS_2 Transistors by Nanoscale Tailoring of Schottky Barrier Using Oxygen Plasma Functionalization. *ACS Appl. Mater. Interfaces* **2017**, *9*, 23164−23174.
(41) Chen, J.; Feng, Z.; Fan, S.; Shi, S.; Yue, Y.; Shen, W.; Xie, Y.; Wu, E.; Sun, C.; Liu, J.; Hao, Z.; Pang, W.; Sun, D.; Feng, W.; Feng, Y.; Sen, W.; Zhang, D. Contact Engineering of Molybdenum Ditelluride Field Effect Transistors through Rapid Thermal Annealing. *ACS Appl. Mater. Interfaces* **2017**, *9*, 30107−30114.

DOI: 10.1021/acsami.8b07196
ACS Appl. Mater. Interfaces 2018, 10, 27840−27849